

# PNAS



## Supporting Information for

### Speckle-correlation imaging through a kaleidoscopic multimode fiber

Dorian Bouchet, Antonio Miguel Caravaca-Aguirre, Guillaume Godefroy, Philippe Moreau, Irène Wang, and Emmanuel Bossy

Corresponding author: Dorian Bouchet

E-mail: [dorian.bouchet@univ-grenoble-alpes.fr](mailto:dorian.bouchet@univ-grenoble-alpes.fr)

#### This PDF file includes:

Figs. S1 to S9  
SI References

## 1. Schematic representation of the optical setup

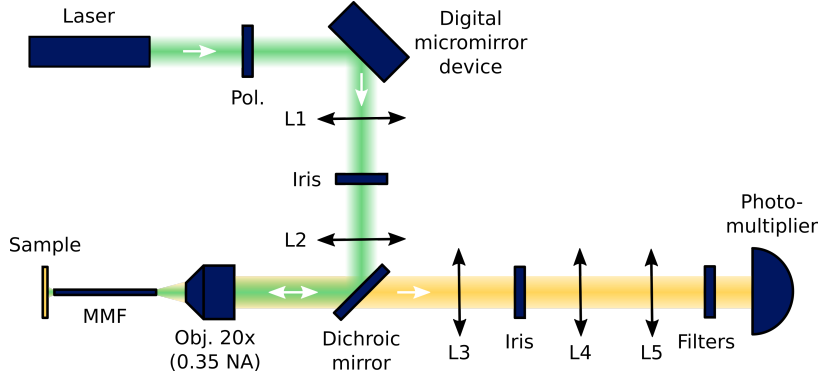


**Fig. S1. Optical setup.** Speckle patterns are generated using a digital micromirror device (DMD) and translated at the input of a square-core multimode fiber. A sample composed of fluorescent beads is placed at the output of the fiber. Fluorescence collected through the fiber passes a dichroic mirror and is detected by a single-channel photomultiplier. MMF: multimode fiber; Pol: linear polarizer; Obj: objective; NA, numerical aperture; L1 to L5, lenses with focal length 300 mm (L1), 150 mm (L2), 200 mm (L3), 100 mm (L4) and 150 mm (L5).

## 2. Calculation of the signal autocorrelation

**A. General expression.** The density distribution of fluorescent emitters  $O(\mathbf{r}_b)$  is related to the measured fluorescence signal  $S(\mathbf{r}_a)$  by the following relation:

$$S(\mathbf{r}_a) = \int O(\mathbf{r}_b) I(\mathbf{r}_a, \mathbf{r}_b) d\mathbf{r}_b, \quad [1]$$

where  $I(\mathbf{r}_a, \mathbf{r}_b)$  is the excitation intensity transmitted at a position  $\mathbf{r}_b$  at the fiber output for a translation  $\mathbf{r}_a$  of the speckle pattern at the fiber input. The statistical autocorrelation function of the fluorescence signal is defined as follows:

$$C_S(\mathbf{r}_a, \mathbf{r}'_a) = \frac{\langle S(\mathbf{r}_a) S(\mathbf{r}'_a) \rangle - \langle S(\mathbf{r}_a) \rangle \langle S(\mathbf{r}'_a) \rangle}{\sqrt{\langle S(\mathbf{r}_a)^2 \rangle - \langle S(\mathbf{r}_a) \rangle^2} \times \sqrt{\langle S(\mathbf{r}'_a)^2 \rangle - \langle S(\mathbf{r}'_a) \rangle^2}}, \quad [2]$$

where  $\langle \dots \rangle$  represents the average over different realizations of the speckle pattern at the fiber input. We also define the contrast of the signal  $K(\mathbf{r}_a)$  as follows:

$$K(\mathbf{r}_a) = \frac{\sqrt{\langle S(\mathbf{r}_a)^2 \rangle - \langle S(\mathbf{r}_a) \rangle^2}}{\langle S(\mathbf{r}_a) \rangle}. \quad [3]$$

Using this definition, Eq. (2) reads

$$C_S(\mathbf{r}_a, \mathbf{r}'_a) = \frac{\langle S(\mathbf{r}_a) S(\mathbf{r}'_a) \rangle - \langle S(\mathbf{r}_a) \rangle \langle S(\mathbf{r}'_a) \rangle}{K(\mathbf{r}_a) \langle S(\mathbf{r}_a) \rangle \times K(\mathbf{r}'_a) \langle S(\mathbf{r}'_a) \rangle}. \quad [4]$$

Using Eq. (1), the average fluorescence signal can be expressed as follows:

$$\langle S(\mathbf{r}_a) \rangle = \langle I(\mathbf{r}_a, \mathbf{r}_b) \rangle \int O(\mathbf{r}_b) d\mathbf{r}_b. \quad [5]$$

Moreover, the correlator  $\langle S(\mathbf{r}_a) S(\mathbf{r}'_a) \rangle$  is given by

$$\langle S(\mathbf{r}_a) S(\mathbf{r}'_a) \rangle = \iint O(\mathbf{r}_b) O(\mathbf{r}'_b) \langle I(\mathbf{r}_a, \mathbf{r}_b) I(\mathbf{r}'_a, \mathbf{r}'_b) \rangle d\mathbf{r}_b d\mathbf{r}'_b. \quad [6]$$

Inserting Eqs. (5) and (6) into Eq. (2) yields

$$C_S(\mathbf{r}_a, \mathbf{r}'_a) = \frac{\iint O(\mathbf{r}_b) O(\mathbf{r}'_b) [\langle I(\mathbf{r}_a, \mathbf{r}_b) I(\mathbf{r}'_a, \mathbf{r}'_b) \rangle - \langle I(\mathbf{r}_a, \mathbf{r}_b) \rangle \langle I(\mathbf{r}'_a, \mathbf{r}'_b) \rangle] d\mathbf{r}_b d\mathbf{r}'_b}{K(\mathbf{r}_a) K(\mathbf{r}'_a) \left[ \int O(\mathbf{r}_b) d\mathbf{r}_b \right]^2 \langle I(\mathbf{r}_a, \mathbf{r}_b) \rangle \langle I(\mathbf{r}'_a, \mathbf{r}'_b) \rangle}. \quad [7]$$

In this expression, we can recognize the definition of the statistical correlation function of the intensity:

$$C_I(\mathbf{r}_a, \mathbf{r}_b, \mathbf{r}'_a, \mathbf{r}'_b) = \frac{\langle I(\mathbf{r}_a, \mathbf{r}_b) I(\mathbf{r}'_a, \mathbf{r}'_b) \rangle - \langle I(\mathbf{r}_a, \mathbf{r}_b) \rangle \langle I(\mathbf{r}'_a, \mathbf{r}'_b) \rangle}{\langle I(\mathbf{r}_a, \mathbf{r}_b) \rangle \langle I(\mathbf{r}'_a, \mathbf{r}'_b) \rangle}. \quad [8]$$

Note that this correlation function is normalized: the speckle is assumed to be fully developed, so that  $\langle I(\mathbf{r}_a, \mathbf{r}_b) \rangle = \sqrt{\langle I(\mathbf{r}_a)^2 \rangle - \langle I(\mathbf{r}_a) \rangle^2}$ . Inserting Eq. (8) into Eq. (7) yields

$$C_S(\mathbf{r}_a, \mathbf{r}'_a) = \frac{\iint O(\mathbf{r}_b)O(\mathbf{r}'_b)C_I(\mathbf{r}_a, \mathbf{r}_b, \mathbf{r}'_a, \mathbf{r}'_b)d\mathbf{r}_bd\mathbf{r}'_b}{K(\mathbf{r}_a)K(\mathbf{r}'_a) [\int O(\mathbf{r}_b)d\mathbf{r}_b]^2}. \quad [9]$$

Shift-shift memory effects (1) (including the translational memory effect observed in square-core fibers) are described by an intensity correlation function  $C_I(\mathbf{r}_a, \mathbf{r}_b, \mathbf{r}'_a, \mathbf{r}'_b) = C_I(\Delta\mathbf{r}_a, \Delta\mathbf{r}_b)$ , where  $\Delta\mathbf{r}_a = \mathbf{r}'_a - \mathbf{r}_a$  and  $\Delta\mathbf{r}_b = \mathbf{r}'_b - \mathbf{r}_b$ . In addition,  $\langle I(\mathbf{r}_a, \mathbf{r}_b) \rangle$  and  $\langle I(\mathbf{r}_a, \mathbf{r}_b)^2 \rangle$  are independent of  $\mathbf{r}_a$  and  $\mathbf{r}_b$ , implying that the signal contrast  $K$  is also independent of  $\mathbf{r}_a$ . This yields

$$C_S(\Delta\mathbf{r}_a) = \frac{\iint O(\mathbf{r}_b)O(\mathbf{r}_b + \Delta\mathbf{r}_b)C_I(\Delta\mathbf{r}_a, \Delta\mathbf{r}_b)d\mathbf{r}_bd\Delta\mathbf{r}_b}{K^2 [\int O(\mathbf{r}_b)d\mathbf{r}_b]^2}. \quad [10]$$

In this expression, we can recognize the spatial autocorrelation function of the object:

$$C_O(\Delta\mathbf{r}_b) = \frac{\int O(\mathbf{r}_b)O(\mathbf{r}_b + \Delta\mathbf{r}_b)d\mathbf{r}_b}{[\int O(\mathbf{r}_b)d\mathbf{r}_b]^2}. \quad [11]$$

Inserting Eq. (11) into Eq. (10) yields

$$C_S(\Delta\mathbf{r}_a) = K^{-2} \int C_O(\Delta\mathbf{r}_b)C_I(\Delta\mathbf{r}_a, \Delta\mathbf{r}_b)d\Delta\mathbf{r}_b. \quad [12]$$

This expression, given as Eq. (2) in the manuscript, relates the autocorrelation function of the fluorescence signal  $C_S(\Delta\mathbf{r}_a)$ , the object autocorrelation function  $C_O(\Delta\mathbf{r}_b)$  and the intensity correlation function of the coherent excitation field  $C_I(\Delta\mathbf{r}_a, \Delta\mathbf{r}_b)$ .

**B. Limiting case.** For an ideal model of square-core fibers with an infinite-range memory effect, the intensity correlation function  $C_I(\Delta\mathbf{r}_a, \Delta\mathbf{r}_b)$  is given by (2)

$$C_I(\Delta\mathbf{r}_a, \Delta\mathbf{r}_b) = \frac{1}{16} \sum_{j=1}^4 \sum_{k=1}^4 C_j(\Delta\mathbf{r}_a, \Delta\mathbf{r}_b)C_k(\Delta\mathbf{r}_a, \Delta\mathbf{r}_b). \quad [13]$$

In this expression, the terms  $C_j$  are field correlation functions defined as follows:

$$C_j(\Delta\mathbf{r}_a, \Delta\mathbf{r}_b) = \frac{2J_1(k_0 \text{NA}) \sqrt{(\Delta x_b - \xi_{x,j}\Delta x_a)^2 + (\Delta y_b - \xi_{y,j}\Delta y_a)^2}}{k_0 \text{NA} \sqrt{(\Delta x_b - \xi_{x,j}\Delta x_a)^2 + (\Delta y_b - \xi_{y,j}\Delta y_a)^2}}, \quad [14]$$

where  $J_1$  is the first-order Bessel function of the first kind,  $k_0 = 2\pi/\lambda$  is the wavenumber, NA is the numerical aperture of the fiber,  $\xi_{x,1} = \xi_{x,3} = \xi_{y,1} = \xi_{y,2} = 1$  and  $\xi_{x,2} = \xi_{x,4} = \xi_{y,3} = \xi_{y,4} = -1$ . Note that field correlation functions defined by Eq. (14) are composed of a single peak. These functions constitute the building blocks of the intensity correlation function given by Eq. (13), which is characterized by four peaks that translate with  $\Delta\mathbf{r}_a$  and that coherently overlap by pair when  $\Delta x_a = 0$  or  $\Delta y_a = 0$ .

Assuming that the correlation functions  $C_j(\Delta\mathbf{r}_a, \Delta\mathbf{r}_b)$  are infinitely sharp (i.e. assuming that the size of the speckle grain is small as compared to the smallest features of the object), we can find approximate expressions for the product  $C_j(\Delta\mathbf{r}_a, \Delta\mathbf{r}_b)C_k(\Delta\mathbf{r}_a, \Delta\mathbf{r}_b)$ . When  $\Delta x_a(\xi_{x,j} - \xi_{x,k}) = 0$  and  $\Delta y_a(\xi_{y,j} - \xi_{y,k}) = 0$ , we can write

$$C_j(\Delta\mathbf{r}_a, \Delta\mathbf{r}_b)C_k(\Delta\mathbf{r}_a, \Delta\mathbf{r}_b) = A\delta(\Delta x_b - \xi_{x,j}\Delta x_a)\delta(\Delta y_b - \xi_{y,j}\Delta y_a), \quad [15]$$

where  $\delta$  denotes the Dirac delta function and  $A = 4\pi/(k_0\text{NA})^2$  is the area covered by a speckle grain. In contrast, when  $\Delta x_a(\xi_{x,j} - \xi_{x,k}) \neq 0$  or  $\Delta y_a(\xi_{y,j} - \xi_{y,k}) \neq 0$ , we can write

$$C_j(\Delta\mathbf{r}_a, \Delta\mathbf{r}_b)C_k(\Delta\mathbf{r}_a, \Delta\mathbf{r}_b) = 0. \quad [16]$$

Using these approximations to calculate the intensity correlation function given by Eq. (13), the signal autocorrelation expressed by Eq. (12) can be simplified as follows:

- when  $\Delta x_a \neq 0$  and  $\Delta y_a \neq 0$ , we have

$$C_S(\Delta\mathbf{r}_a) = \frac{A}{16K^2} [C_O(\Delta x_a, \Delta y_a) + C_O(-\Delta x_a, \Delta y_a) + C_O(\Delta x_a, -\Delta y_a) + C_O(-\Delta x_a, -\Delta y_a)]; \quad [17]$$

- when  $\Delta x_a = 0$  and  $\Delta y_a \neq 0$ , we have

$$C_S(\Delta\mathbf{r}_a) = \frac{A}{4K^2} [C_O(\Delta x_a = 0, \Delta y_a) + C_O(\Delta x_a = 0, -\Delta y_a)]; \quad [18]$$

- when  $\Delta x_a \neq 0$  and  $\Delta y_a = 0$ , we have

$$C_S(\Delta \mathbf{r}_a) = \frac{A}{4K^2} [C_O(\Delta x_a, \Delta y_a = 0) + C_O(-\Delta x_a, \Delta y_a = 0)]; \quad [19]$$

- when  $\Delta x_a = 0$  and  $\Delta y_a = 0$ , we have

$$C_S(\Delta \mathbf{r}_a) = \frac{A}{K^2} C_O(\Delta x_a = 0, \Delta y_a = 0). \quad [20]$$

Since  $C_O$  is an even function, we can write  $C_O(\Delta x_a, \Delta y_a) = C_O(-\Delta x_a, -\Delta y_a)$  and  $C_O(\Delta x_a, -\Delta y_a) = C_O(-\Delta x_a, \Delta y_a)$ . Defining  $C_O^{\text{sym}}(\Delta \mathbf{r}_a) = [C_O(\Delta x_a, \Delta y_a) + C_O(\Delta x_a, -\Delta y_a)]/2$  as the symmetrized version of the object autocorrelation, we obtain

$$C_S(\Delta \mathbf{r}_a) = \frac{A}{K^2} \times \begin{cases} C_O^{\text{sym}}(\Delta \mathbf{r}_a)/4 & \text{if } \Delta x_a \neq 0 \text{ and } \Delta y_a \neq 0, \\ C_O^{\text{sym}}(\Delta \mathbf{r}_a)/2 & \text{if } \Delta x_a = 0 \text{ and } \Delta y_a \neq 0, \\ C_O^{\text{sym}}(\Delta \mathbf{r}_a)/2 & \text{if } \Delta x_a \neq 0 \text{ and } \Delta y_a = 0, \\ C_O^{\text{sym}}(\Delta \mathbf{r}_a) & \text{if } \Delta x_a = 0 \text{ and } \Delta y_a = 0. \end{cases} \quad [21]$$

This expression shows that, in the limiting case of an infinite-range memory effect with a speckle grain size approaching zero, the signal autocorrelation can be written as  $C_S(\Delta \mathbf{r}_a) \propto w(\Delta \mathbf{r}_a) C_O^{\text{sym}}(\Delta \mathbf{r}_a)$ , where  $w$  is a weight function that is equal to 1 if  $\Delta x_a = 0$  and  $\Delta y_a = 0$ , to 1/2 if either  $\Delta x_a = 0$  or  $\Delta y_a = 0$ , and to 1/4 otherwise.

### 3. Intensity correlation function of square-core multimode fibers

In the experiment, due to the limited range of the kaleidoscopic memory effect, the intensity correlation function  $C_I(\Delta \mathbf{r}_a, \Delta \mathbf{r}_b)$  differs from the one predicted by the ideal model [see Eqs. (13) and (14)]. To experimentally measure this correlation function,

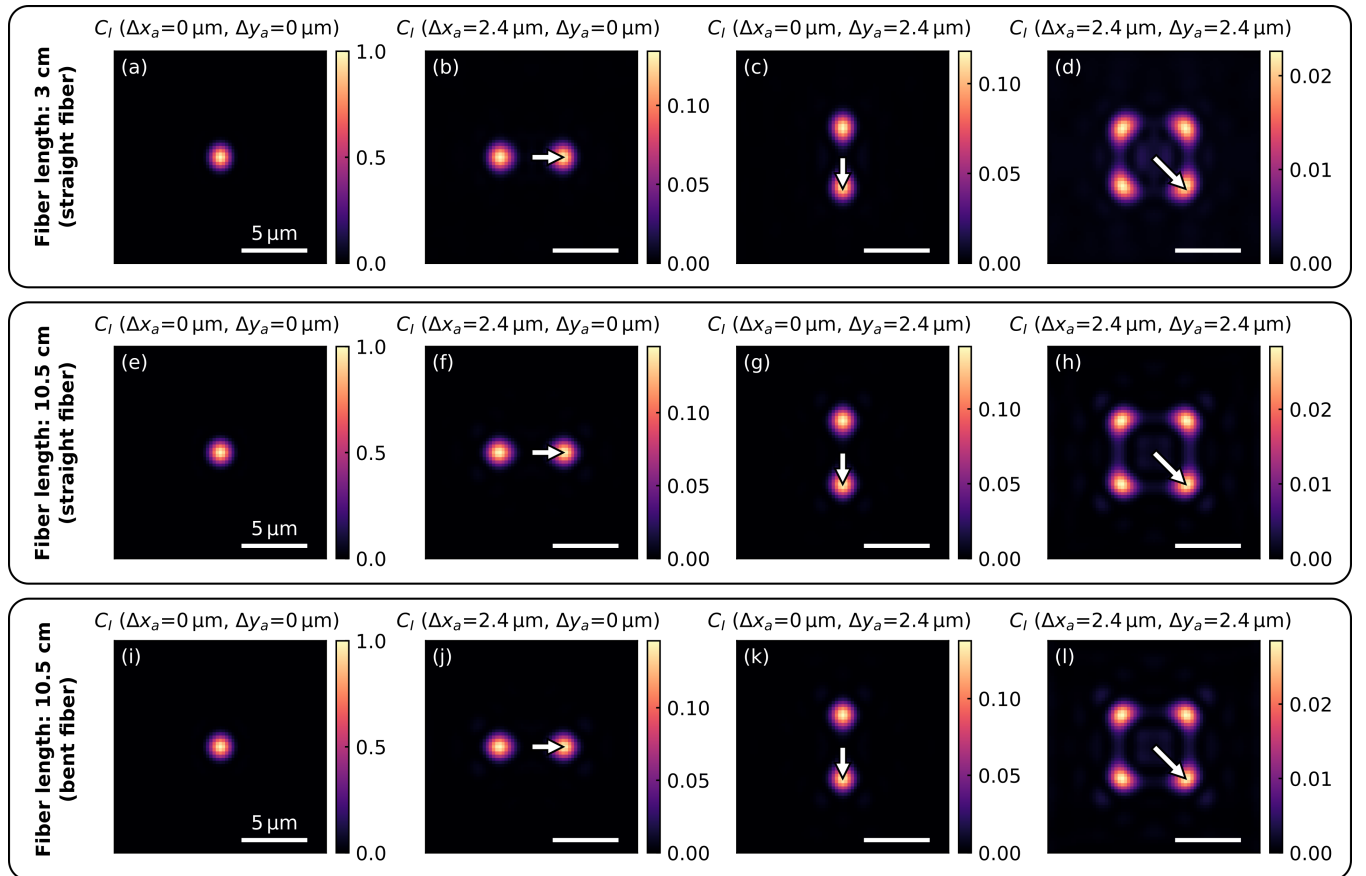


**Fig. S2.** (a-d) Intensity correlation function of the excitation field  $C_I(\Delta \mathbf{r}_a, \Delta \mathbf{r}_b)$  for the 3 cm long fiber, held in a straight position. The correlation function is represented as a function of  $\Delta \mathbf{r}_b$  (shift at the fiber output) for four different values of  $\Delta \mathbf{r}_a$  (shift at the fiber input, represented by the white arrows on the figures). (e-h) Analogous to (a-d) for the 10.5 cm long fiber, held in a straight position. The range of the memory effect is not visibly affected by the longer length of the fiber (the observed range is even slightly larger). (i-l) Analogous to (a-d) for the 10.5 cm long fiber, held deformed. While this deformation fully decorrelates output speckle patterns, the range of the memory effect is not visibly affected by the fiber bending. Note that there is a twist of  $5.5^\circ$  between the input and the output planes of the 10.5 cm long fiber; this angle is however not visible in the figures, as the coordinates  $\Delta \mathbf{r}_b$  are defined in the rotated frame.

we imaged the intensity of the coherent field at the fiber output using a  $\times 20$  objective (Mitutoyo Plan Apo SL 20X/0.28) along with a 200 mm lens and a CMOS camera (Basler acA1300-200um). We generated 10,000 random realizations of the input field, we translated them with the DMD ( $\mathbf{r}_a$  covers a  $8\ \mu\text{m} \times 8\ \mu\text{m}$  area), and we recorded the intensity measured by the camera ( $\mathbf{r}_b$  covers a  $14.6\ \mu\text{m} \times 14.6\ \mu\text{m}$  area). The normalized intensity correlation function  $C_I(\Delta\mathbf{r}_a, \Delta\mathbf{r}_b)$  is then calculated from its definition [see Eq. (8)], averaging over all possible spatial pairs and all realizations of the input field. Finally, we take advantage of known symmetries and average the calculated normalized intensity correlation function with its left-right flipped version and its up-down flipped version, both on the input side and on the output side. As a result, we obtain the correlation function shown in Fig. S2a-d in the case of the 3 cm long fiber (also shown in Fig. 2d-g of the manuscript), and the correlation function shown in Fig. S2e-h in the case of the 10.5 cm long fiber. These correlation functions are very similar, indicating that the kaleidoscopic memory effect is robust in this range of fiber lengths. Finally, after perturbing the 10.5 cm long fiber by applying a displacement  $\delta = 100\ \mu\text{m}$  at mid-length, we obtain the correlation function shown in Fig. S2i-l. While this perturbation leads to a full decorrelation of the output speckle patterns (see Supplementary Section 8), the intensity correlation function  $C_I(\Delta\mathbf{r}_a, \Delta\mathbf{r}_b)$  remains the same before and after the deformation, demonstrating that the memory effect is robust to such a perturbation. Note that, in the case of the 10.5 cm long fiber, the fiber was naturally twisted by an angle of  $5.5^\circ$ . In such a case, the memory effect follows the axes of the fiber, without any visible reduction in the range covered by the effect.

#### 4. Inherent ambiguities in the inverse problem

There are several possible solutions when trying to retrieve  $O(\mathbf{r}_b)$  from  $C_O^{\text{sym}}(\Delta\mathbf{r}_b)$ . First, as in usual inverse autocorrelation problems, any shift of the object in the transverse plane leads to the same symmetrized autocorrelation function. Moreover, since  $C_O^{\text{sym}}(\Delta x_b, \Delta y_b) = C_O^{\text{sym}}(-\Delta x_b, \Delta y_b) = C_O^{\text{sym}}(\Delta x_b, -\Delta y_b) = C_O^{\text{sym}}(-\Delta x_b, -\Delta y_b)$ , there exists four different objects that lead to the same symmetrized autocorrelation. These four objects are flipped versions of each other, as illustrated in Fig. S3. Note that a similar ambiguity also exists in usual inverse autocorrelation problems (3): since  $C_O(\Delta x_b, \Delta y_b) = C_O(-\Delta x_b, -\Delta y_b)$ , there exists two different objects that lead to the same autocorrelation (the two objects that are represented in Fig. S3a and Fig. S3d).

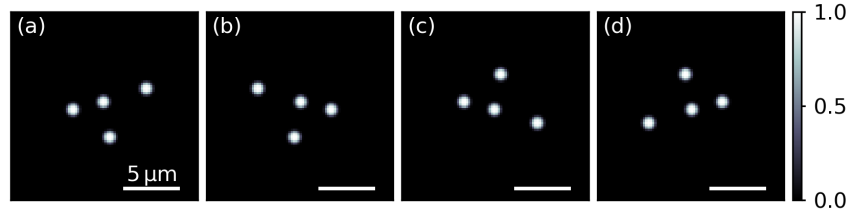


Fig. S3. Ambiguities in the inverse problem. These four different objects, that are flipped versions of each other, lead to the same symmetrized autocorrelation.

#### 5. Influence of statistical fluctuations on the reconstructed images

In order to minimize the influence of statistical fluctuations on the reconstructed images, the measured signal autocorrelation is averaged over random realizations of the input field. In the manuscript, we presented data obtained with  $N_{\text{rep}} = 40,000$ , yielding a signal correlation with no visible artifacts but requiring a significant acquisition time (4 hours in total). Nevertheless, information about the object is still available even for much lower numbers of realizations. To illustrate this, we compare in Fig. S4 signal autocorrelations and reconstructed images for different numbers of realizations of the input field.

- For  $N_{\text{rep}} = 200$  (acquisition time of 1 min 12s), the shape of the objects is not faithfully reconstructed, but some distinctive features already appear on the signal autocorrelations (Fig. S4a,e,i).
- For  $N_{\text{rep}} = 3,000$  (acquisition time of 18 min), the shape of the objects can already be recognized, but a few beads are slightly mislocalized. In this case, signal autocorrelations strongly resemble the theoretical predictions (Fig. S4d,h,l), even though artifacts can be observed on the edge of the autocorrelations—edges are more sensitive to statistical fluctuations, as they benefit from a weaker spatial averaging effect.
- For  $N_{\text{rep}} = 40,000$  (acquisition time of 4 hours), no artifacts due to statistical fluctuations can be observed, and the position of the beads is correctly retrieved (Fig. S4c,g,k).

Note that objects with a large number of beads are typically more sensitive to statistical fluctuations, and it can happen that, even for a large number of realizations of the input field, two different beads configurations lead to similar signal autocorrelations that are hard to separate, preventing us to robustly image objects with large numbers of beads using the current reconstruction procedure.

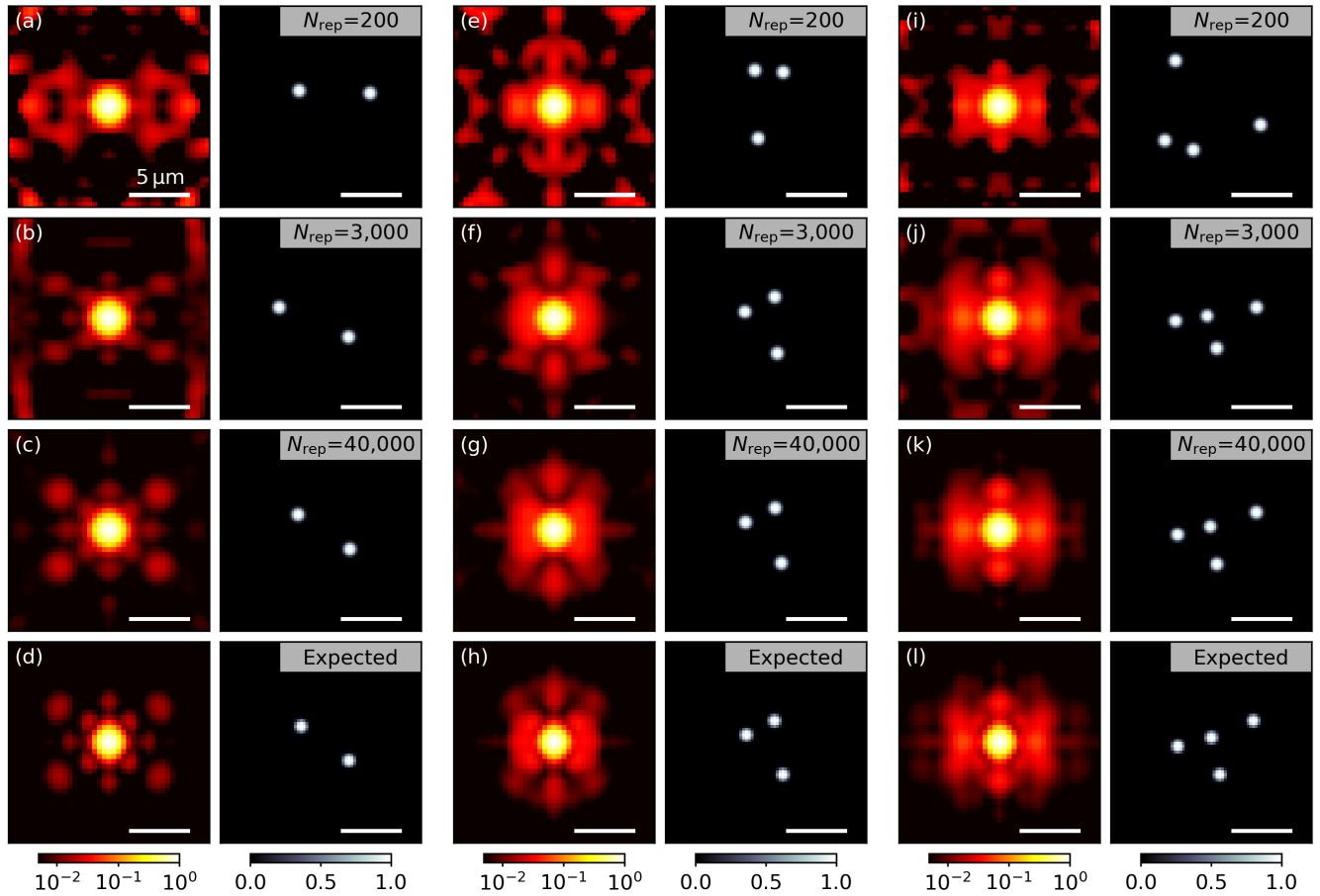


**Fig. S4.** Signal autocorrelations retrieved from experimental measurements and reconstructed images for different numbers of realizations of the input field. (a-c) Signal autocorrelation (top) and reconstructed images (bottom) for the sample composed of two beads, for  $N_{rep} = 200$  realizations (a),  $N_{rep} = 3,000$  (b) and  $N_{rep} = 40,000$  (c). (d) Theoretically-predicted signal autocorrelation (left) along with the true position of the beads (right). (d-h) Analogous to (a-d) for the object composed of three fluorescent beads. (i-l) Analogous to (a-d) for the object composed of four fluorescent beads.

## 6. Determination of the number of fluorescent beads

In principle, the number of fluorescent beads could be determined directly from the measured signal autocorrelation. Nevertheless, a more robust strategy consists in analyzing the statistics of the measured signal. The voltage distribution associated with the fluorescence signal measured through the 3 cm long fiber is shown in Fig. S5, for the three objects shown in the manuscript (composed of 2, 3 and 4 beads, respectively). For comparison purposes, we also present the distribution obtained in the case of 0 and 1 bead. The average value of these distributions is proportional to the number of beads, with approximately 0.40 V for each bead. Experimentally, we observed average values of 0.87 V for the object composed of 2 beads, 1.17 V for the object

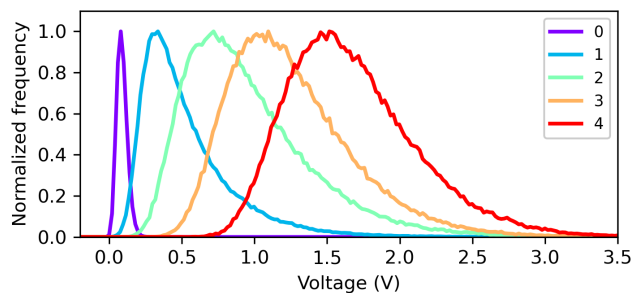


**Fig. S5.** Statistics of the measured fluorescence signal for different numbers of beads. Voltage distribution associated with the fluorescence signal measured through the 3 cm long fiber, for a number of beads ranging from 0 to 4. Both the average value and the contrast of these distributions can be used to determine the number of beads.

composed of 3 beads and 1.60 V for the object composed of 4 beads, which allowed us to correctly infer the number of beads from these measurements.

Note that another strategy would consist in analyzing the contrast of the measured signals, defined as the ratio between the standard deviation and the average value of the fluorescence signal. In theory, the contrast is equal to  $1/\sqrt{n}$  for  $n$  point-like fluorescent emitters (4). Contrasts measured in our experiment do not reach this theoretical limit, which is expected as the size of the beads ( $1.0\ \mu\text{m}$  in diameter) is comparable to that of the speckle grain ( $0.5\lambda/\text{NA} = 1.2\ \mu\text{m}$ ). Nevertheless, observed contrasts do decrease with the number of beads; for the data presented in Fig. S5, the contrast is 0.71 for 1 bead, 0.50 for 2 beads, 0.37 for 3 beads and 0.28 for 4 beads. This indicates that analyzing the contrast is also a possible strategy to determine the number of beads (using e.g. a suitable theoretical model).

## 7. Image reconstruction of fluorescent beads from experimental measurements

Our reconstruction procedure is based on three essential features: the processing of the experimental data, the implementation of the theoretical model, and the optimization algorithm.

**A. Processing of the experimental data.** The fluorescence signal is experimentally measured for  $N_{\text{rep}} = 40,000$  realizations of the input field. For each realization, we sequentially construct a  $21 \times 21$  image by translating the input speckle pattern over an area of  $8\ \mu\text{m} \times 8\ \mu\text{m}$  and by measuring the resulting intensity with the photomultiplier (Fig. S6a). This signal is known to be band-limited in the spatial domain due to the finite size of the speckle grain; thus, we apply a Gaussian spatial filter to the measured signal in order to reduce fluctuations arising from measurement noise (Fig. S6b). Due to the significant acquisition time, we also observed a slow decay of the average signal measured by the photomultiplier, which can be due to laser power fluctuations and to the slow photobleaching of the beads (Fig. S6c). Therefore, we fit a function based on cubic splines to the temporal dependence of the signal, and we use this function to compensate for this decay (Fig. S6d). The normalized signal autocorrelation function  $C_S(\Delta\mathbf{r}_a)$  is then directly calculated from its definition [see Eq. (2)], averaging over all possible spatial pairs and all realizations of the input field. Finally, we take advantage of the known symmetry of the signal autocorrelation function and average the calculated signal autocorrelation with its left-right flipped version (or, equivalently, with its up-down flipped version), which further reduces the influence of statistical fluctuations. As a result, we obtain the signal correlation function estimated from experimental measurements, that we denote  $C_S^{\text{meas}}(\Delta\mathbf{r}_a)$ .

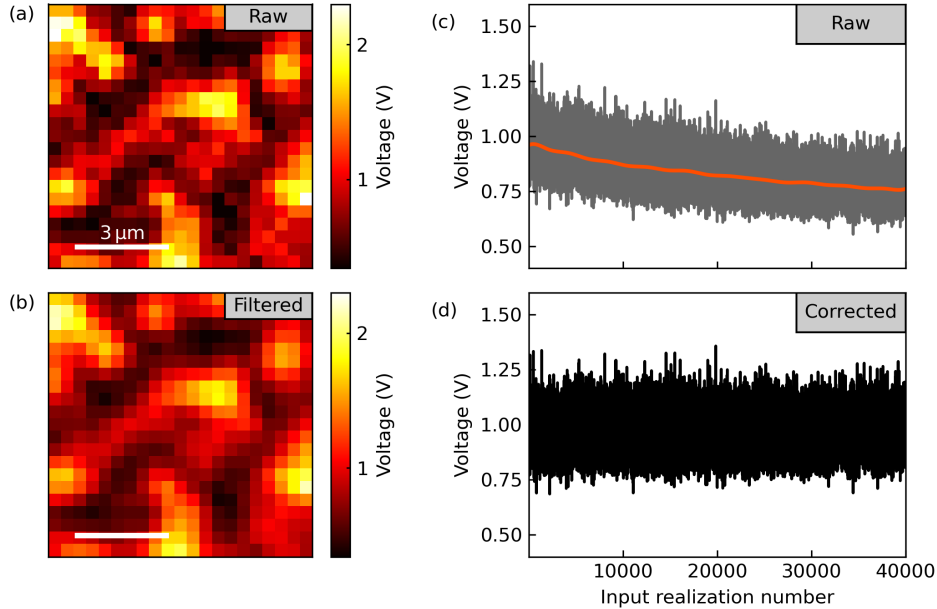


**Fig. S6.** Processing of measured experimental data. (a) Example of a raw fluorescence signal measured by the photomultiplier as a function of  $\Delta\mathbf{r}_a$ , shown here for the object composed of 2 beads. (b) Same signal as in (a) after being smoothed by a Gaussian spatial filter, that we used to reduce the influence of measurement noise. (c) Average signal measured by the photomultiplier as a function of the number of realizations of the input field (gray curve), along with a model function (orange curve) based on cubic splines. (d) Same signal as in (c) after being compensated for the observed decay.

**B. Implementation of the theoretical model.** In order to theoretically predict the signal autocorrelation from Eq. (12), we must develop a model for the object function  $O(\mathbf{r}_b)$ . For this purpose, we model fluorescent beads as high-order Gaussian functions, with the same amplitude for all beads and a full width at half maximum equal to  $1\ \mu\text{m}$  (i.e. the known diameter of the beads). The object function  $O(\mathbf{r}_b)$  is constructed by summing all contributions from the beads (see Fig. 2b of the manuscript), and its spatial autocorrelation  $C_O(\Delta\mathbf{r}_b)$  is numerically calculated from  $O(\mathbf{r}_b)$  (see Fig. 2c of the manuscript). In addition to  $C_O(\Delta\mathbf{r}_b)$ ,

the theoretical expression of the signal autocorrelation also involves the intensity correlation function  $C_I(\Delta\mathbf{r}_a, \Delta\mathbf{r}_b)$ . While we could use the expression of  $C_I(\Delta\mathbf{r}_a, \Delta\mathbf{r}_b)$  that was obtained based on an ideal model of square-core fibers [see Eqs. (13) and (14)], this would not take into account the limited range of the memory effect that we experimentally observed. For this reason, we estimate  $C_I(\Delta\mathbf{r}_a, \Delta\mathbf{r}_b)$  from experimental measurements, for both the 3 cm long fiber and the 10.5 cm long fiber (see Supplementary Section 3). Finally, the signal autocorrelation is calculated from  $C_O(\Delta\mathbf{r}_b)$  and  $C_I(\Delta\mathbf{r}_a, \Delta\mathbf{r}_b)$  using Eq. (12). As a result, we obtain the predicted signal correlation function (see Fig. 2i of the manuscript), that we denote  $C_S^{\text{pred}}(\Delta\mathbf{r}_a)$ .

**C. Optimization algorithm.** Our reconstruction algorithm is based on the minimization of a loss function that compares theoretical predictions to measured data. As the signal correlation significantly decays with the distance  $\Delta\mathbf{r}_a$ , and since the positions of the beads is typically encoded into large values of  $\Delta\mathbf{r}_a$ , our loss function is defined using the logarithm of  $C_S^{\text{meas}}(\Delta\mathbf{r}_a)$  and  $C_S^{\text{pred}}(\Delta\mathbf{r}_a)$ , which efficiently increases the contribution of the most useful parts of the signal correlation function. However, this strategy also tends to increase the contribution of artifacts that are due to statistical fluctuations. Thus, we define a fixed threshold  $C_{\text{min}}$  below which values of  $C_S^{\text{meas}}(\Delta\mathbf{r}_a)$  are considered as artifacts and are not taken into account for the calculation of the loss function. Denoting  $\tilde{C}_S^{\text{meas}}(\Delta\mathbf{r}_a)$  and  $\tilde{C}_S^{\text{pred}}(\Delta\mathbf{r}_a)$  the functions  $C_S^{\text{meas}}(\Delta\mathbf{r}_a)$  and  $C_S^{\text{pred}}(\Delta\mathbf{r}_a)$  defined on the restricted domain for which  $C_S^{\text{meas}}(\Delta\mathbf{r}_a) \geq C_{\text{min}}$ , we use the following loss function:

$$L(\theta) = \left\| \log[\tilde{C}_S^{\text{meas}}(\Delta\mathbf{r}_a)] - \log[\tilde{C}_S^{\text{pred}}(\Delta\mathbf{r}_a, \theta)] \right\|^2 + R_{\text{fov}}(\theta) + R_{\text{dmin}}(\theta) + R_{\text{dmax}}(\theta), \quad [22]$$

where  $\|\dots\|$  denotes the Euclidean distance (i.e. the L2 norm),  $\theta = \{x_i, y_i\}_{i=1, \dots, n}$  denotes the positions of the  $n$  beads, and  $R_{\text{fov}}(\theta)$ ,  $R_{\text{dmin}}(\theta)$ , and  $R_{\text{dmax}}(\theta)$  denote three regularization terms. The first regularization term  $R_{\text{fov}}(\theta)$  is an exponential potential that penalizes beads located outside the predefined field of view ( $10 \mu\text{m} \times 10 \mu\text{m}$ ). The second regularization term  $R_{\text{dmin}}(\theta)$  is an exponential potential function that penalizes beads that are too close to each other. In this way, we ensure that two beads cannot overlap. The third regularization term  $R_{\text{dmax}}(\theta)$  is an exponential potential function that penalizes beads that are too far apart, based on the area for which  $\tilde{C}_S^{\text{meas}}(\Delta\mathbf{r}_a)$  is defined. In this way, the distance between two beads is restricted to the area for which measured values of the signal correlation function are significant.

The cost function defined by Eq. (22) is not convex, and must therefore be minimized using a global optimization strategy. To this end, we implemented an algorithm based on simulated annealing, which is an optimization algorithm inspired by statistical mechanics (5). Starting with a random guess for the beads positions, the algorithm typically converges after  $200 \times p$  iterations, where  $p$  is the number of parameters to be estimated (i.e. twice the number of beads since two coordinates must be estimated for each bead). To increase the probability that the global minimum was reached, we repeated this procedure for 20 different random initial guesses, and we kept the solution that yielded the lowest value of the loss function. In the case of the 3 cm long fiber, the number of times that the algorithm converged to this optimal solution was 12/20 for the object composed of 2 beads, 16/20 for the object composed of 3 beads, and 3/20 for the object composed of 4 beads. In the case of the dynamically-perturbed 10.5 cm long fiber, the number of times that the algorithm converged to this optimal solution was respectively 2/20 and 10/20 for the two objects composed of 4 beads. Overall, this indicates that the inverse problem tends to become more difficult to be solved when increasing the number of beads. Note that the algorithm frequently reconstructs flipped versions of the objects, which is expected due to the known ambiguity in the inverse problem (see Supplementary Section 4). In the manuscript, reconstructed images were presented by selecting the version that best corresponds to the ground truth among the 4 possibilities.

## 8. Speckle decorrelation induced by perturbing the fiber

In order to quantitatively assess the influence of the perturbation induced by the rod upon the transmission matrix of the imaging system, we generate a random speckle pattern at the fiber input and we measure output speckle patterns for different displacements  $\delta$  of the rod. We then calculate the spatial cross-correlation  $\mathcal{C}(\Delta x, \Delta y)$  of the measured patterns for these

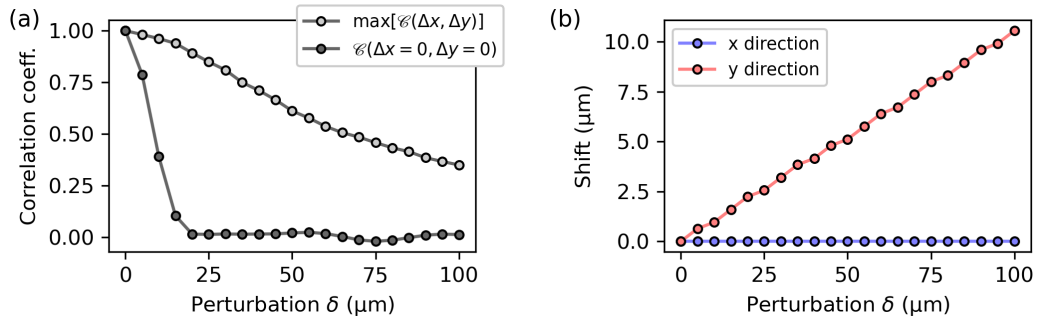


**Fig. S7.** (a) Correlation coefficient as a function of the applied perturbation, taking as a reference the speckle pattern measured for  $\delta = 0 \mu\text{m}$ . The correlation coefficient evaluated at zero shift  $\mathcal{C}(\Delta x = 0, \Delta y = 0)$  includes the effect of speckle decorrelation and of the transverse shift of the fiber output, while the maximum of the correlation coefficient  $\max[\mathcal{C}(\Delta x, \Delta y)]$  includes only the effect of speckle decorrelation. (b) Transverse shift of the fiber output as a function of the applied perturbation, calculated from the position of the maximum value of  $\mathcal{C}(\Delta x, \Delta y)$ .

different values of  $\delta$ , taking as a reference the pattern measured for  $\delta = 0 \mu\text{m}$ . The value of  $\mathcal{C}(\Delta x = 0, \Delta y = 0)$  decreases from one to zero for a displacement of the rod of approximately  $20 \mu\text{m}$  (Fig. S7a, dark points), evidencing that the transmission matrix of the imaging system is completely modified by a perturbation  $\delta \geq 20 \mu\text{m}$ .

The observed perturbation of the transmission matrix is due not only to a decorrelation of the speckle patterns but also to a transverse shift of the fiber. In order to disentangle the influence of these two effects, we calculate the maximum value of the function  $\mathcal{C}(\Delta x, \Delta y)$  for each value of the perturbation  $\delta$  (Fig. S7a, light points). We observe that the value of  $\max[\mathcal{C}(\Delta x, \Delta y)]$  also decreases with  $\delta$ , reaching a value of 0.35 for  $\delta = 100 \mu\text{m}$ . This indicates that the modification of the transmission matrix of the imaging system is not entirely due to the decorrelation of the speckle patterns, but that it is also partly due to a transverse shift of the fiber. This is confirmed by studying the shift of the fiber output as a function of  $\delta$  (Fig. S7b), which occurs in the direction of the displacement of the rod inducing the perturbation (the  $y$  direction) and reaches a value of  $10.6 \mu\text{m}$  for  $\delta = 100 \mu\text{m}$ .

We emphasize that, since both the decorrelation of the speckle patterns and the transverse shift of the fiber modify the transmission matrix of the imaging system, the relevant metric to quantify the influence of the perturbation is here  $\mathcal{C}(\Delta x = 0, \Delta y = 0)$ , which is represented by the dark points in Fig. S7a and which is also shown in Fig. 4e of the manuscript.

## 9. Image reconstruction through a 10.5 cm long fiber with and without dynamic perturbations

To further demonstrate that the dynamical aspect of the applied perturbation does not significantly influence the efficiency of the method, we present here complementary experimental results obtained from the objects that we presented in Fig. 4 of the manuscript. However, instead of dynamically-perturbing the fiber, we maintained the fiber in a static position (Fig. S8, top row). Both the measured signal autocorrelations and the reconstructed images are very similar to the results obtained using a dynamically-perturbed fiber (Fig. S8, bottom row). This confirms that, while some stability is required when scanning a given input speckle pattern (220 ms in our experiments), the fiber can be perturbed between different random realizations of the input speckle pattern without affecting the efficiency of the method.

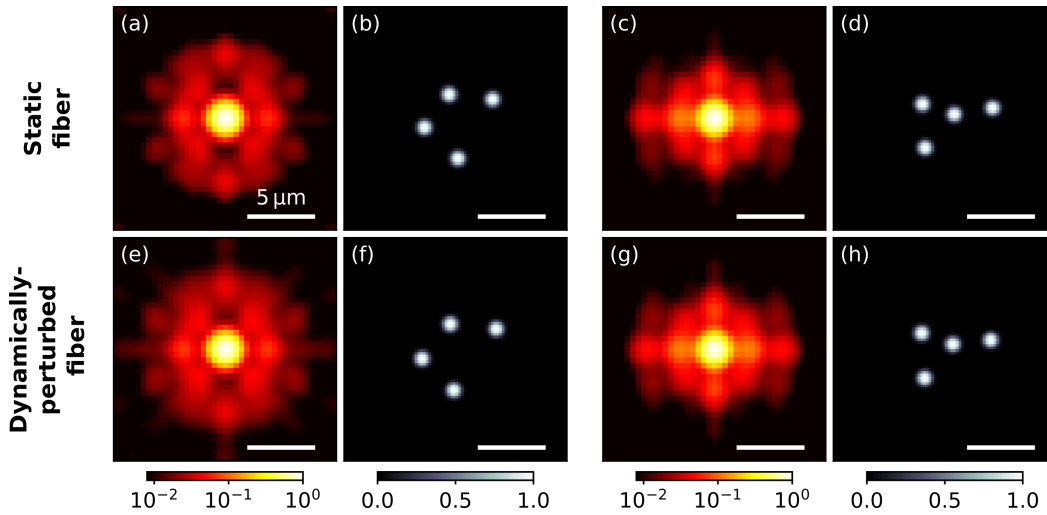


**Fig. S8.** (a) Signal autocorrelation retrieved from experimental measurements (averaged over  $N_{\text{rep}} = 40,000$  speckle illuminations), for the object presented in Fig. 4g of the manuscript. For these measurements, the 10.5 cm long fiber was maintained in a static position. (b) Reconstructed images of the beads. (c-d) Analogous to (a-b) for the object presented in Fig. 4h of the manuscript. (e-h) Signal autocorrelations and reconstructed images of the beads from experimental measurements performed while dynamically perturbing the fiber. Note that these results are those presented from Fig. 4k to Fig. 4n in the manuscript.

## 10. Image reconstruction of handwritten digits from numerical simulations

To complement the results presented in Fig. 4 of the manuscript, we show in Fig. S9 additional simulation results. In this figure, the top row is composed of objects extracted from the test set, the middle row is composed of the associated signal autocorrelations, and the bottom row is composed of the predicted images reconstructed by the artificial neural network. In one of these examples (the one associated with the digit 5), the image was not properly reconstructed, illustrating the fact that the procedure is not error-free. However, over the whole test set, the average structural similarity is 0.89, which indicates that the predictions generally strongly resemble the ground truths. In addition, we trained a classifier using signal autocorrelations as inputs, which yields a success rate of 91%. Overall, these results demonstrate the strong potential of artificial neural networks to successfully solve the inverse problem and reconstruct images based on measured signal autocorrelations.

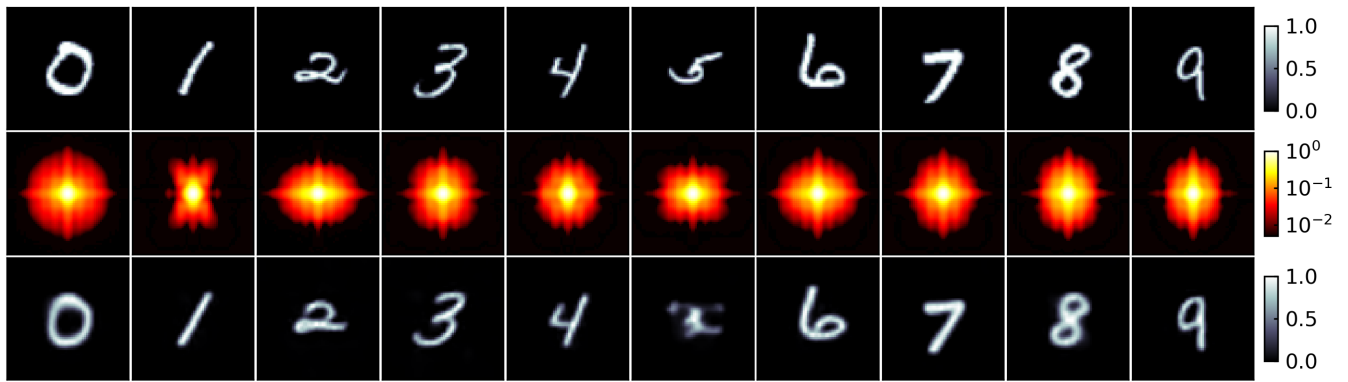


**Fig. S9.** Reconstructed images of handwritten digits in numerical simulations (see also Fig. 4 of the manuscript). First row: Grayscale images from the MNIST database of handwritten digits, that are used as objects in our numerical simulations. Second row: Signal autocorrelations of these objects calculated using Eq. (12). Third row: Images reconstructed by an artificial neural network, demonstrating that the inverse problem can be successfully solved even in the case of complicated objects. In one of these examples (the one associated with the digit 5), the image was not properly reconstructed, illustrating the fact that the procedure is not error-free.

## References

1. G Osnabrugge, R Horstmeyer, IN Papadopoulos, B Judkewitz, IM Vellekoop, Generalized optical memory effect. *Optica* **4**, 886–892 (2017).
2. AM Caravaca-Aguirre, A Carron, S Mezil, I Wang, E Bossy, Optical memory effect in square multimode fibers. *Opt. Lett.* **46**, 4924–4927 (2021).
3. J Bertolotti, et al., Non-invasive imaging through opaque scattering layers. *Nature* **491**, 232–234 (2012).
4. O Krichevsky, G Bonnet, Fluorescence correlation spectroscopy: the technique and its applications. *Rep. Prog. Phys.* **65**, 251–297 (2002).
5. S Kirkpatrick, CD Gelatt, MP Vecchi, Optimization by Simulated Annealing. *Science* **220**, 671–680 (1983).